Nanoscale Advances

ROYAL SOCIETY OF CHEMISTRY

PAPER

View Article Online
View Journal | View Issue

Cite this: *Nanoscale Adv.*, 2026, **8**, 3234

Photodegradation of indigo carmine over a $(BiO)_2CO_3$@$ZnCo_2O_4$ heterojunction: experimental and DFT insights

Nguyen Thi Mai Tho, *[a] Nguyen Quoc Thang, [a] Minh An Tran Nguyen, [a] Nguyen Thi Hong Anh [b] and Nguyen Le Kim Phung[c]

This work effectively synthesized the novel heterojunction $(BiO)_2CO_3$@$ZnCo_2O_4$ using precipitation and co-precipitation methods facilitated by microwave and ultrasonic techniques. The crystal structure and morphology of the synthesized samples were characterized by X-ray diffraction (XRD), Fourier-transform infrared spectroscopy (FT-IR), ultraviolet-visible diffuse reflectance spectroscopy (UV-vis DRS), X-ray Photoelectron Spectroscopy (XPS), scanning electron microscopy (SEM), energy-dispersive X-ray spectroscopy (EDX), and energy-dispersive spectroscopy (EDS) mapping, respectively. The photodegradation effectiveness of the heterojunction was evaluated by degrading the indigo carmine dye under visible light. The research findings demonstrated that the combination of $(BiO)_2CO_3$ and $ZnCo_2O_4$ at a mass ratio of 12% exhibited the most significant IC decomposition capability, attaining a photocatalytic efficiency of 98.6% after 60 minutes in darkness and 100 minutes of light exposure. The most appropriate approach was to establish a first-order kinetic model for the indigo carmine degrading process of $(BiO)_2CO_3$@$ZnCo_2O_4$. The Z-scheme mechanism was more relevant than the conventional type-II heterojunction, whereby $O_2^{\bullet-}$ and $^{\bullet}OH$ were the primary contributors to the photocatalytic process. The stable heterostructure $(BiO)_2CO_3$@$ZnCo_2O_4$ has advanced the method for effective heterojunction photocatalysis. DFT–Fukui analysis shows that the indigo carmine molecule donates electrons, acting as a nucleophile, and TD-DFT calculations using B3LYP/6-311G(d,p) in aqueous solution produce a HOMO–LUMO gap for IC that aligns more closely with experimental data than previous results.

Received 31st January 2026
Accepted 25th March 2026

DOI: 10.1039/d6na00080k

rsc.li/nanoscale-advances

1. Introduction

Contamination of water by industrial wastewater discharge has become a major global environmental problem. Hazardous contaminants such as halogens, heavy metal ions, and artificial colours that are difficult to break down in natural settings are frequently found in industrial effluents.[1] Indigo Carmine (IC), a prevalent pollutant, is extensively utilised in the textile industry and is commonly found in wastewater. Because of its persistent aromatic structure and sulfonate functional groups, IC is resistant to traditional chemical and biological treatment methods. It can harm human health and aquatic habitats.[2,3] Therefore, the removal of this persistent dye from wastewater has drawn significant attention to the development of effective treatment methods, especially advanced oxidation processes (AOPs). A variety of semiconductors have been evaluated as testing photocatalysts, including TiO_2, ZnO, SnO_2, Cu_2O, and Fe_2O_3 oxides,[4] oxide mixes ($CuFe_2O_4$, $ZnFe_2O_4$, $CoFe_2O_4$, $MnCo_2O_4$, and $ZnCo_2O_4$)[5], poly metallates ($BiVO_4$, Bi_2WO_6, and $SrTiO_3$),[6] and chalcogenides (MoS_2, CdS, and Bi_2S_3).[7,8] Nonetheless, the efficacy of photocatalytic processes remains suboptimal, either due to a high band gap energy preventing light absorption, too low energy facilitating rapid recombination of photogenerated electrons and holes, or instability leading to solubility issues and the generation of hazardous by-products during the photocatalytic process.[6] The addition of doping metals and/or the combination of various semiconductors, to enhance the photocatalytic efficacy of the heterojunction, facilitates the integration of advantageous characteristics from each constituent compound, extends the absorption range within the visible spectrum, diminishes photoexcited electron–hole recombination, and augments photochemical stability.[4,9,10] The construction of heterojunctions in photocatalysts is one of the most promising methods for preparing advanced and efficient photocatalysts.[11]

$ZnCo_2O_4$ is a typical spinel material characterised by its unique electronic structure, extensive specific surface area, excellent electrochemical performance, and p-type

[a]Faculty of Chemical Engineering, Industrial University of Ho Chi Minh City, Ho Chi Minh, Vietnam
[b]Faculty of Chemical Engineering, Ho Chi Minh City University of Industry and Trade, 140 Le Trong Tan Street, Tay Thanh Ward, Ho Chi Minh 70000, Vietnam
[c]Institute of Science and Technology for Energy and Environment – Viet Nam Academy of Science and Technology, A30 Building, No. 18 Hoang Quoc Viet, Nghia Do Ward, Hanoi, Vietnam

semiconducting nature, exhibiting many morphologies, including nanocubes,[12] nanospheres,[13] nanosheets, and nanowires.[14] This specific band structure facilitates intrinsic electron transitions, decreasing the recombination rate of photogenerated electron–hole pairs. $ZnCo_2O_4$ has a small band gap (1.77–2.01 eV) and may absorb visible light, but readily facilitates recombination between electrons and holes, making it a good candidate for the development of effective heterojunctions with other photocatalysts.[15,16] Masoud Salavati Niasari and colleagues established graphene oxide (GO) onto $ZnCo_2O_4$ nanospheres to develop an effective photocatalyst for pollutant degradation under visible light exposure.[13] The results indicated that GO/$ZnCo_2O_4$ (mass ratio of GO/$ZnCo_2O_4$ = 25%) had the highest organic degradation efficiency, achieving 94.3% during 120 minutes of visible light exposure. Eric W. Cochran successfully synthesised CuO/$ZnCo_2O_4$/CNTs *via* sol–gel and co-precipitation methods. The photocatalytic findings indicated that CuO/$ZnCo_2O_4$/CNTs had the capacity to destroy over 87.7% of CV dye, 82% of diclofenac sodium, and 72% of phenol. The enhanced performance of the CNT-based composite results from the synergistic interaction between CuO/$ZnCo_2O_4$ nanocomposites and CNTs. Consequently, the synthesised CuO/$ZnCo_2O_4$/CNTs photocatalyst can efficiently decompose organic wastewater.[5] Furthermore, several other studies are also noteworthy, including those on ZnO/$ZnCo_2O_4$,[17] $CaFe_2O_4$/$ZnCo_2O_4$ and SnO_2/$ZnCo_2O_4$.[18]

Recently, several researchers have investigated bismuth-based photocatalysts owing to their comparatively high photocatalytic efficacy, including $BiVO_4$, Bi_2WO_6, BiOX (X = Cl, Br, I), $Bi_{12}SiO_{20}$, and Bi_2MoO_6.[19,20] Among these photocatalysts, n-type semiconductor $(BiO)_2CO_3$, which has a layered structure whereby the CO_3^{2-} group is orientated perpendicularly to the $[Bi_2O_2]^{2+}$, is considered suitable for photocatalytic applications due to its exceptional properties.[20] However, the practical application of $(BiO)_2CO_3$ photocatalysts under sunlight is limited due to their wide band gap (≈3.3–3.5 eV), which allows absorption mainly in the ultraviolet region. To overcome this, various methods have been investigated, including elemental doping, heterostructure construction, and recombination of other multifunctional materials such as Bi_2S_3/$(BiO)_2CO_3$,[21] and TiO_2/$CuBi_2O_4$/$(BiO)_2CO_3$.[22]

By increasing charge separation and light absorption, heterostructure systems have been widely recognised as an efficient way to overcome the limitations of pure semiconductors. The direct Z-scheme heterostructure is particularly appealing, as it preserves the robust redox properties of charge carriers while inhibiting electron–hole recombination. Despite numerous reports on Z-scheme photocatalysts, the advancement of efficient ZC-based heterostructure systems with enhanced charge-transport characteristics remains underexplored. This work successfully created a heterogeneous $(BiO)_2CO_3$/($ZnCo_2O_4$) photocatalyst and thoroughly investigated its photocatalytic effectiveness for IC dye degradation. In addition, the Fukui theory, based on the Density Function Theory (DFT), was applied and HOMO–LUMO-DFT boundary orbitals were calculated in aqueous solvent to analyse the physicochemical properties of dye degradation, the local reactivity of atoms in IC, and the global reactivity of IC in heterostructure photocatalysis.

2. Experimental section

2.1 Synthesis of composites

2.1.1 Preparation of $ZnCo_2O_4$. 50 mL of NaOH 0.5 M solution was slowly added at a rate of 2 mL min^{-1} into solution B, which comprises 100 mL of $Co(NO_3)_2$ 0.2 M and $Zn(CH_3COO)_2$ 0.1 M in a molar ratio of Co^{2+}/Zn^{2+} of 2/1. The reaction was conducted in an ultrasonic bath operating at 35 kHz and maintained at a pH of 9–10 until completion. The mixture was ultrasonicated for 30 minutes after the response is complete to obtain a pink suspension. The mixture was placed in a flask and refluxed for 60 min in a microwave oven (Toshiba MWP-MM20P(WH)). The product was subjected to filtration and multiple washes with water, followed by drying at 105 °C for 6 hours and heating at 600 °C for 3 hours to yield a black powder called ZC.

2.1.2 Preparation of $(BiO)_2CO_3$@$ZnCo_2O_4$. 1.91 g of $Bi(NO_3)_3 \cdot 5H_2O$ and 0.3 g of citric acid were dissolved in 60 mL of 5% HNO_3 to prepare solution A. Solution A was added to mixture B, which contains *m* (g) of ZC uniformly distributed in 60 mL of Na_2CO_3 containing 0.4 M, at a 2 mL min^{-1} rate.[20] Mixture B was reacted in an ultrasonic tank (operating at 35 kHz) and the pH was stabilized at 8–9 during the reaction. To maintain a stable pH in the optimal range (8–9), a dilute NaOH solution (0.05 N) was introduced dropwise in small amounts as needed. After the response, mixture B was continued to be ultrasonicated for 1 hour and then transferred to a flask and recirculated at 80 °C for an additional 2 hours to stabilize the structure. The precipitate was filtered, washed many times for purification, and dried at 80 °C to obtain the product. By adjusting the mass *m* (g) of ZC to match the mass ratios of $(BiO)_2CO_3$/$ZnCo_2O_4$ products at 6%, 12%, and 18% labeled 6BiC@ZC, 12BiC@ZC, and 18BiC@ZC will be produced. The synthesis of $(BiO)_2CO_3$ was conducted similarly to the process above, using solution B and excluding the mass of ZC, referred to as BiC.

2.2 Photocatalytic degradation of IC

The photocatalytic efficacy of BiC@ZC samples was assessed using the IC dye under visible light. The reactions occurred within a catalytic system comprising two glass layers: the inner layer contained a defined volume of dye solution, while the outer layer circulated water to maintain a temperature of 30 °C throughout the photocatalytic process. The catalytic system was agitated at a velocity of 500 rpm throughout the reaction, both in darkness and under light exposure. The photocatalytic experiment was conducted as outlined below:

m grams of catalyst and 100 mL of IC solution at a specified concentration (C_{in}) were introduced into the inner layer of the catalyst system, and the mixture was stirred for 60 minutes in darkness to achieve equilibrium/desorption. 3 mL of the suspension was aspirated from the system and filtered through a 0.22 μm filter to remove the catalyst; the resultant solution

after filtration provides the IC concentration (C_0). A 300 W halogen lamp (Osram, Germany, model 64640 HLX 150 W, 24 V) that emits visible light without a filter was used to directly illuminate the catalyst system, holding the suspension mixture, for 100 minutes. To examine the influence of time on photocatalytic efficiency, a 3 mL sample is extracted and filtered every 20 minutes, after which the concentration (C_t) is measured.

The concentration of the IC solution was ascertained spectrophotometrically, with a peak wavelength of 665 nm. The influence of the BiC/ZC mass ratio, catalyst dosage, dye concentration and pH on the IC breakdown process of BiC@ZC was studied. Furthermore, investigations on reactive species and reuse were conducted for the BiC@ZC heterogeneous catalyst. The trials were conducted separately and replicated three times ($n = 3$), with the average result used for the computations.

Using experimental data on the change in the IC concentration over photocatalytic duration, we used apparent kinetic equations of zero, first, and second orders to model and assess the kinetics of IC breakdown of BiC@ZC over time. In this context, k_0, k_1, and k_2 represent the rate constants for zero, first, and second order reactions.

$$C_t - C_0 = k_0 t, \quad \ln\left(\frac{C_0}{C_t}\right) = k_1 t, \quad \frac{1}{C_t} - \frac{1}{C_0} = k_2 t$$

2.3 Procedure for the Fukui function and frontier MOs of IC

To determine which colours and pharmacological compounds break down easily and which ones are more challenging, *in silico* researchers have performed physicochemical calculations for degradation using the Fukui theory.[23,24] To make accurate predictions about the local reactivity of atoms and molecules, the Fukui function, derived from the conceptual Density Functional Theory (DFT), is a powerful statistical tool. The Fukui function calculation method: the IC structure was computed using Gaussian 09 (IA32W-G09RevD) using a single-point energy calculation, theory: B3LYP, and basis set: 6-31G(d,p). The output adheres to the standard *Z*-matrix format (compact) and is derived from the IC.chk file. In the DFT calculation with Gaussian 09W, IC.com inputs the necessary parameters for the IC molecule into Gaussian View, employing the keywords #b3lyp/6-31g(d), scrf=(smd, solvent=water), pop=(full,nbo,savenbos), and iop(3/33=4). The output files of the DFT method have been identified through the IC.chk and IC.log files. The IC.chk file has been processed using the Gaussian 09W software through the Utilities menu, and the formchk command has been executed to generate the IC.fch file.[25] The IC.fch and IC.log files are designated as the input files for UCA-Fukui software version 2. The results of the calculations can be found in the fukuiI.res and fukuiII.res files. Frontier molecule orbital, HOMO–LUMO method: the structure of IC was optimised using Avogadro software, saved as IC.com, and analysed *via* the DFT method concentrated on frontier orbitals (HOMO–LUMO) in aqueous media, utilising the B3LYP functional and the 6-31G(d) basis set from Gaussian 09W software.[26]

3. Results and discussion

3.1 Structure and morphology

X-ray diffraction (XRD) was used to study the phase composition of the materials, as seen in Fig. 1A. ZC, synthesised by the co-precipitation method followed by calcination at 500 °C, showed peaks at 19.06°, 31.24°, 36.73°, 44.65°, 55.56°, 59.2° and 65.09° corresponding to the (111), (220), (311), (400), (422), (511), and (440) planes of $ZnCo_2O_4$ (JCPDS 23-1390), respectively.[27] The BiC sample displays diffraction peaks at 12.9°; 24.01°; 26.65°; 30.36°; 32.91°; 35.17°; 39.58°; 42.41°; 47.02°; 48.05°; 53.53° and 56.89°; corresponding to the (002); (011); (004); (013); (110); (112); (006), (114); (020); (022); (024) and (123) lattice planes characteristic of a tetragonal $(BiO)_2CO_3$ structure.[21,28]

On dispersing BiC onto the ZC surface at mass ratios of 6%, 12%, and 18% (6BiC@ZC, 12BiC@ZC, and 18BiC@ZC), the diffraction analysis revealed that all 3 samples exhibited characteristic peaks of ZC; however, the intensity of the principal peaks progressively diminished in comparison to ZC due to the interaction with BiC.[28] In the 6BiC@ZC and 12BiC@ZC samples, no peaks indicative of the $(BiO)_2CO_3$ phase were seen, suggesting that the level of the $(BiO)_2CO_3$ phase was much lower than the $ZnCo_2O_4$ level, resulting in the absence of peak intensity. This also indicates that BiC was well disseminated on the ZC substrate. Specifically for the 18BiC@ZC sample, with the distinctive peaks of ZC, the principal peaks of BiC are also present.

The FT-IR data for the BiC, ZC, and BiC@ZC samples are shown in Fig. 1B. ZC exhibits two peaks at 574 and 652 cm^{-1}, indicating the Co–O stretching and Zn–O vibration in spinel $ZnCo_2O_4$.[16] BiC exhibits peaks at 1432–1337 cm^{-1} and 810 cm^{-1}, indicative of the stretching vibration of the CO_3^{2-} group, whereas the stretching band of Bi–O–Bi is seen at around 547 cm^{-1}.[28,29] The 6BiC@ZC, 12BiC@ZC, and 18BiC@ZC samples also show the vibrations of Bi–O–Bi and CO_3^{2-} in addition to the distinctive peaks that indicate the M–O vibration of the ZC sample; the greater the BiC amount, the more pronounced the intensity of these peaks became, XRD and FT-IR measurements indicated the successful synthesis of the BiC@ZC heterojunction.

A strong light absorption capacity is advantageous for semiconductors, as it facilitates the efficient stimulation of photogenerated electrons. UV-vis DRS diffuse reflectance spectra were obtained to examine the light absorption capacity of the produced compounds. Fig. 2A illustrates that white BiC has a strong absorption edge in the ultraviolet spectrum at a wavelength of 410 nm, while black ZC demonstrates total absorption from the ultraviolet to the visible spectrum.[30,31] Previous studies indicate that $ZnCo_2O_4$ has a structure characterized by high-spin tetrahedral Zn^{2+} ($e_g^4t_{2g}^2$) and low-spin octahedral Co^{3+} (t_{2g}^6).[13,32] The band structure of $ZnCo_2O_4$ is established by designating the O 2p orbital as the valence band and the Co 3d orbital as the conduction band, resulting in a unique internal electronic transition. Upon light absorption, electrons may (1) transition from the O 2p orbital to Co 3d-e_g; (2)

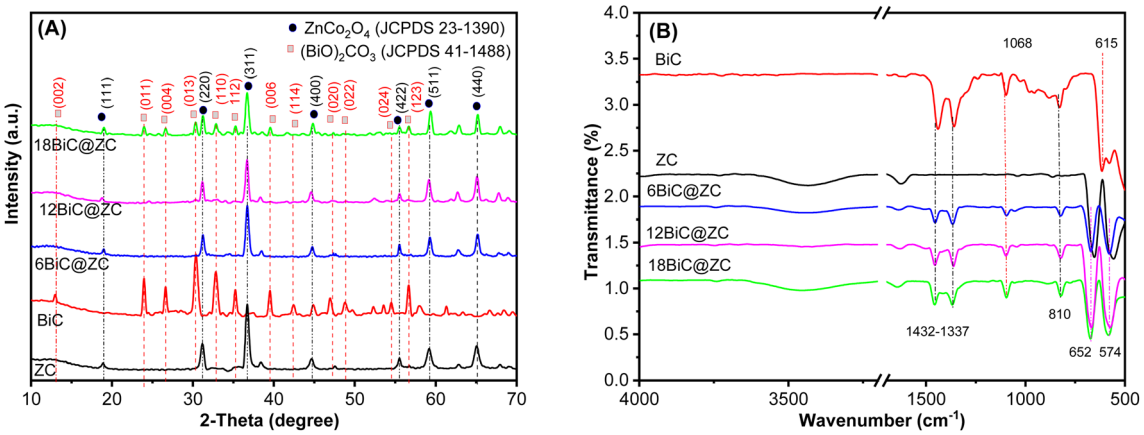

Fig. 1 Characteristics of the prepared materials. (A) XRD patterns and (B) FT-IR spectra of ZC, BiC, 6BiC@ZC, 12BiC@ZC, and 18BiC@ZC.

transition from O 2p to Co 3d-t_{2g}; and (3) transition from Co 3d-t_{2g} to Co 3d-e_g.[33] The band gap energy (E_g) of ZC is ascertained to be 1.67 eV using the Tauc plot function (Fig. 2B), indicative of type 2 photoexcitation (O 2p to Co 3d-t_{2g}).[34] The BiC@ZC sample exhibits an interaction between BiC and ZC that alters the absorption wavelength; the O 2p electrons of $ZnCo_2O_4$ in the BiC@ZC sample may be transported by (1), (2), or (3).[32] The absorption wavelengths of 6BiC@ZC, 12BiC@ZC, and 18BiC@ZC exhibit a red shift relative to ZC, with values of 587, 624, and 635 nm^{-1}, respectively. This alteration is ascribed to the robust interaction between BiC and ZC, which modifies the inherent electronic transfer capacity of ZC in BiC@ZC, thereby changing the light absorption ability of the heterojunction.

Fig. 2C displays the photoluminescence (PL) results of ZC and 12BiC@ZC when stimulated at a wavelength of 285 nm. The most significant intensity peak, located at around 322 nm, was detected in both samples. The PL spectra of ZC revealed a high emission peak intensity, which may indicate low photocatalytic effectiveness due to strong recombination between electron and hole energy bands. The emission peak intensity of the 12BiC@ZC sample decreased markedly, indicating a significant reduction in recombination and suggesting that this composite possesses visible-light photocatalytic potential.[35,36]

Fig. 3A–F displays the XPS spectrum that analyzes the surface state and chemical makeup of the 12BiC@ZC and ZC samples.[37] The full survey findings reveal that the ZC sample consists of three elements: Co, Zn, and O, while the BiC@ZC sample includes Bi, C, Co, Zn, and O (Fig. 3A). Both samples exhibit the absence of foreign elements, indicating that the synthesized substance is pure and free from contaminants.

The high-resolution spectrum of the BiC@ZC sample reveals the Bi 4f spectrum (Fig. 3B) with two energy levels at 158.60 eV and 163.94 eV, corresponding to Bi^{3+} $4f_{7/2}$ and Bi^{3+} $4f_{5/2}$.[37,38] The C 1s spectrum (Fig. 3C) is deconvoluted into three peaks at 284.43 eV (C=C), 285.09 eV (C–O), and 288.5 eV (C=O), signifying the presence of CO_3^{2-} bonds within the layered structure of $(BiO)CO_3$.[28,37] The binding energies of Zn $2p_{3/2}$ and Zn $2p_{1/2}$, representative of Zn^{2+} in the two samples 12BiC@ZC and ZC,[14] are shown in Fig. 3D. The Zn 2p peaks of the sample 12BiC@ZC exhibit positive shifts of 0.51 eV and 0.64 eV, respectively, compared to the Zn $2p_{3/2}$ (1021.36 eV) and Zn $2p_{1/2}$ (1043.95 eV) peaks of the sample ZC. The high-resolution Co 2p XPS spectra exhibit two peaks with binding energies of 778.98 eV and 794.04 eV, suggestive of Co^{3+}, and two peaks at 780.14 and 795.23, representative of Co^{2+}, characteristic of cobalt oxide spinel. In addition, the spectrum reveals two satellite peaks, sat 1 and sat 2, indicating the multivalent state of Co in spinel

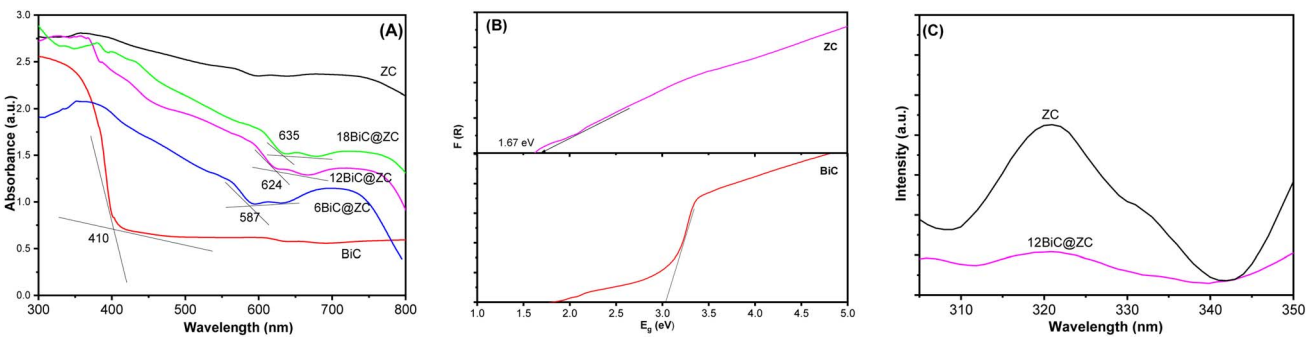

Fig. 2 Characteristics of the prepared materials. (A) UV-vis DRS of BiC, 6BiC@ZC, 12BiC@ZC, 18BiC@ZC, and ZC. (B) The corresponding Tauc's plots of ZC and BiC. (C) PL of ZC and 12BiC@ZC.

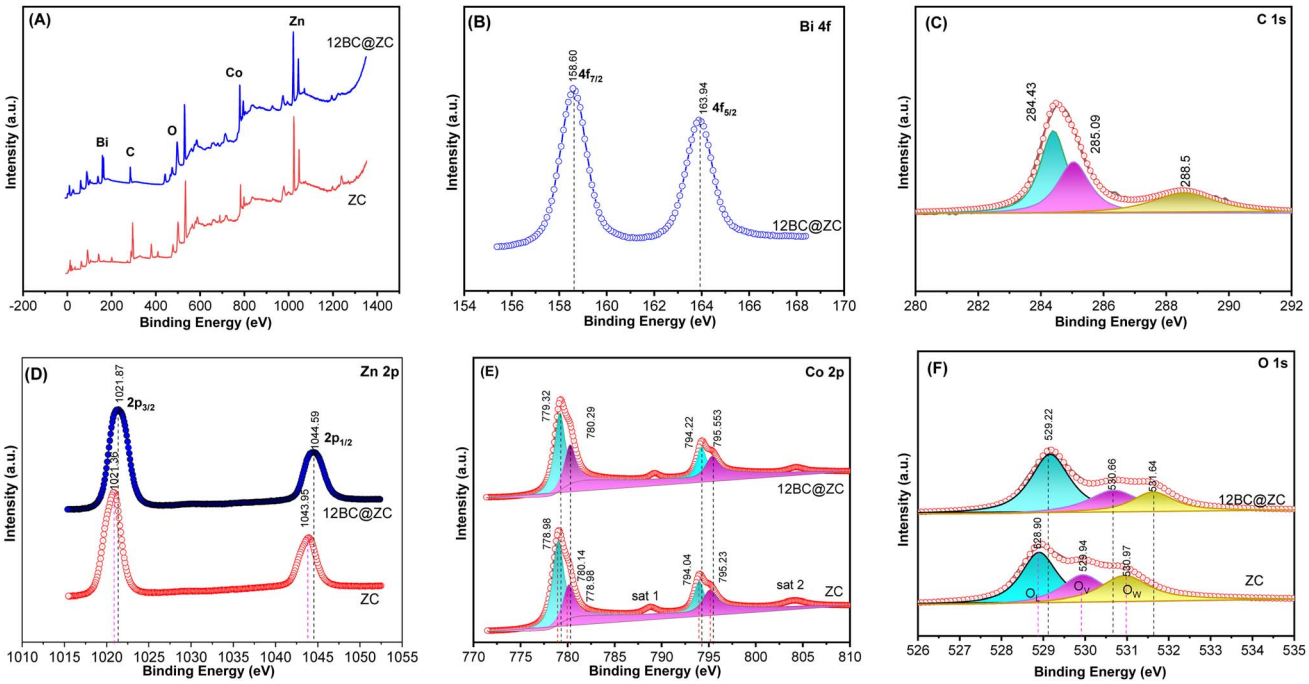

Fig. 3 XPS spectra of ZC and 12BiC@ZC catalysts: (A) survey spectrum, (B) Bi 4f; (C) C 1s; (D) Zn 2p; (E) Co 2p; (F) O 1s.

$ZnCo_2O_4$.[30,39] The binding energy of Co 2p in sample 12BiC@ZC exceeds that of Co 2p in sample ZC (Fig. 3E). The deconvolution of the O 1s peak (Fig. 3F) reveals three peaks at 528.90, 529.94, and 530.97 eV, which correspond to the metal–oxygen bond (O_L), a significant presence of oxygen vacancies (O_V), and O–H groups that adsorb water on the ZC surface (O_w).[31,39] Similar to Zn 2p and Co 2p, the O 1s of the 12BiC@ZC sample exhibits a positive shift relative to the O 1s of the ZC sample. The alteration in binding energy of Zn 2p, Co 2p, and O 1s leads to a variation in electron cloud density on the ZC surface, showing a robust chemical interaction between BiC and ZC in the 12BiC@ZC sample. This chemical interaction creates an efficient charge transfer bridge at the heterojunction of the two phases, BiC and ZC, thereby diminishing the recombination of electrons and photogenerated holes and enhancing photocatalytic efficiency.[38]

Fig. 4A–E displays SEM images of the BiC, ZC, and BiC@ZC samples. The BiC imaging findings indicate that the morphology of the nano-fragments is uneven, with the nanosheets layered and dispersed in a distinct and heterogeneous fashion. Conversely, ZC has a diminutive size ranging from around 10 to 50 nm, exhibits a spherical morphology, and is densely aggregated. Spreading BiC to the ZC surface in varying mass ratios demonstrates that ZC clings randomly to the BiC layers, minimizing agglomeration. The increased BiC amount correlates with enhanced ZC dispersion capability. Samples 12BiC@ZC and 18BiC@ZC demonstrate that many BiC voids remain inadequately distributed by ZC, establishing advantageous circumstances for the aggregate reduction process, facilitating light absorption, and augmenting the photochemical efficacy of the @ZC. As shown in Fig. 4F and G, TEM and HRTEM were used to further highlight the heterojunction structure. The dark and bright colours that cross ZC and BiC show that there were many ZC nanoparticles scattered on the BiC surface that were closely related to one another. Additionally, the crystal lattice spacing was clearly defined as 0.29 nm and 0.25 nm, corresponding to the (110) crystal plane of $(BiO)_2CO_3$ (ref. 35) and the (311) crystal plane of $ZnCo_2O_4$,[16] respectively. This result showed that a tight interface was formed, indicating that the BiC@ZC heterojunction was successfully synthesised.

The EDX and EDX mapping of the 12BiC@ZC sample (Fig. 4H) showed that, apart from the elements Co (33.41 wt%), Zn (7.17 wt%), O (30.35 wt%), C (7.17 wt%), and Bi (3.02 wt%), no other elements appeared, proving that the synthesis process of 12BiC@ZC had high purity and no impurities.

3.2 Photocatalytic performance

Fig. 5A and B illustrate the photocatalytic efficacy of BiC, ZC, and BiC@ZC in the degradation of the IC dye. The findings reveal that the synthesized materials can adsorb IC, processing 15–20% of IC during 60 minutes of light off. Upon exposure to a halogen lamp simulating visible light for 100 minutes, the results show that BiC and ZC exhibit poor IC breakdown efficiency, processing just 27.9% and 60.2%, respectively. This result matches the light absorption capacity of BiC and ZC as ascertained by UV-vis DRS. BiC mostly absorbs light in the UV spectrum. ZC absorbs light efficiently in the visible light spectrum, but photogenerated electrons and holes recombine more frequently.[16] The amalgamation of BiC and ZC in various mass ratios significantly enhanced the IC decomposition efficiency of 6BiC@ZC, 12BiC@ZC, and 18BiC@ZC to 91.9%, 98.6%, and

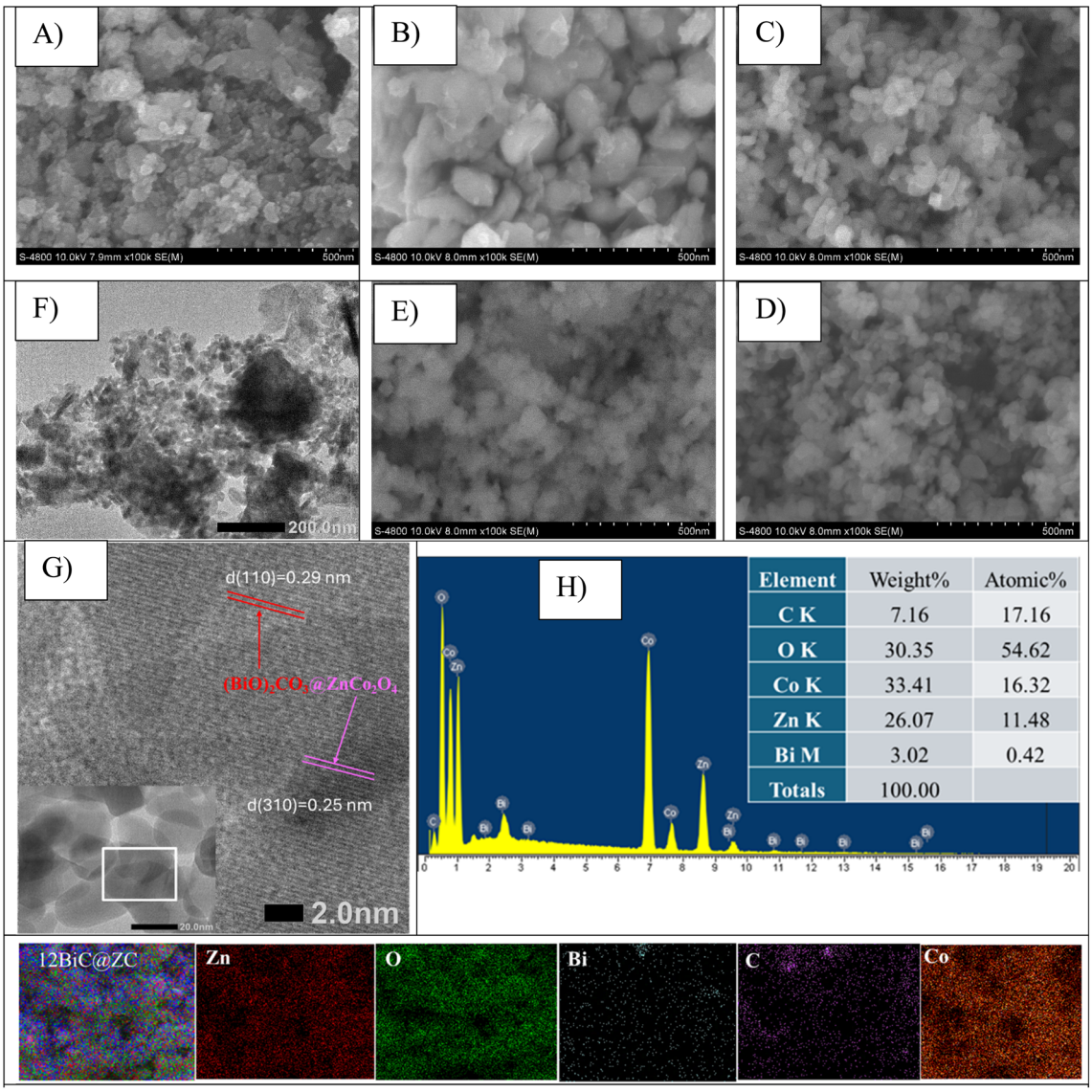

Fig. 4 SEM images of (A) ZC, (B) BiC, (C) 6BiC@ZC; (D) 12BiC@ZC; (E) 18BiC@ZC. (F and G) TEM and HRTEM images; (H) EDX and EDX mapping of 12BiC@ZC.

94.3%, respectively. Furthermore, the UV-vis DRS and PL results indicate that the combination reduced the disadvantages of the two pure materials, increased the absorption of light for BiC, established an intermediary layer between the two phases, generated a synergistic effect, enhanced effective charge separation, and inhibited recombination, thereby increasing the formation of reactive oxygen species (ROS) and promoting the decomposition of IC. The SEM image findings of BiC@ZC indicated that ZC was uniformly distributed on the BiC surface, thereby minimizing the likelihood of ZC aggregation and augmenting the photocatalytic efficacy.

Nevertheless, the IC decomposition efficiency is also influenced by the combination ratio of BiC and ZC. The 12BiC@ZC sample with insufficient BiC loading is inadequate for optimal heterojunction formation, leading to rapid recombination or excessive BiC relative to ZC, which diminishes light absorption. By conducting a benchmarking experiment with TiO_2 under the same experimental conditions, the photocatalytic activity of 12BiC@ZC was evaluated. The results showed that after 100 minutes of irradiation, the BiC@ZC composite achieved 98.6% IC degradation, while TiO_2 degradation reached approximately 91.8%. Importantly, 12BiC@ZC showed a faster breakdown rate than TiO_2 within the 60 minutes of irradiation. Table 1 presents a comparison of the pollutant degradation efficiency of BiC@ZC with that of previously examined $ZnCo_2O_4$-based photocatalysts.

Fig. 5C–E and Table 2 illustrate the zero-order, first-order, and second-order kinetic equations related to the IC breakdown of the synthesized materials. Table 2 presents the data from the linear regression analysis, along with the corresponding rate constants (k_0, k_1, and k_2) as determined using the zero-order, first-order, and second-order equations for the IC

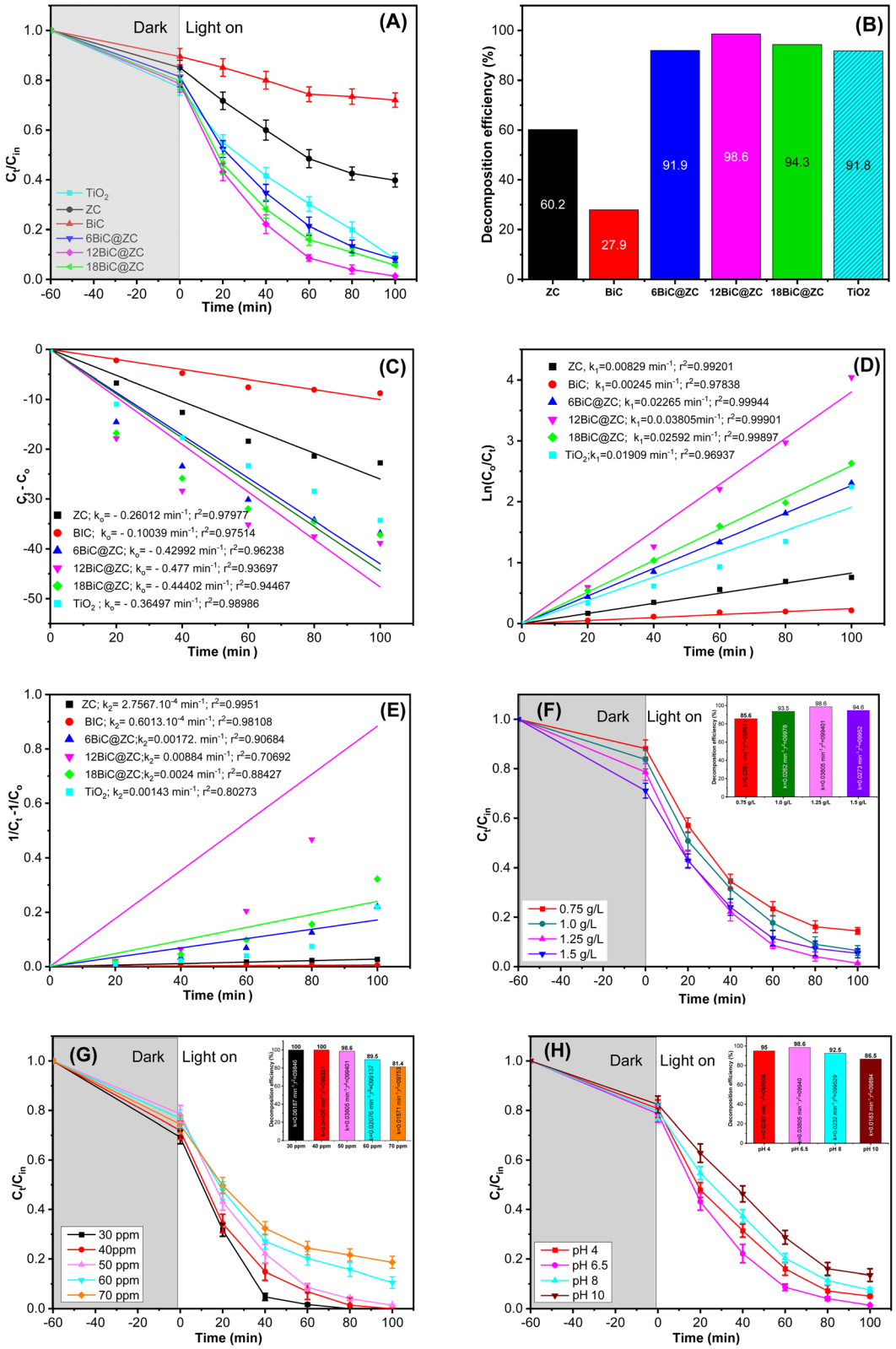

Fig. 5 (A and B) Photocatalytic degradation plots, (C) zero-order kinetics plots, (D) first-order kinetics plots, and (E) second-order kinetics plots of ZC, BiC@ZC, and BiC; (F) effect of catalyst dosage; (G) effect of initial concentration IC; (H) effect of pH.

breakdown of the materials. Comparing the r^2 values of r_0^2 = 0.97977–0.93697, r_1^2 = 0.97838–0.99901, and r_2^2 = 0.9951–0.88427 indicates that the simulation of IC breakdown using the first-order kinetic equation is the most appropriate. The rate constant k_1 of 12BiC@ZC is 4.6 times greater than the constant k_1 of ZC. As per the first-order kinetic equation, the IC

Table 1 Comparative analysis of $ZnCo_2O_4$-based photocatalysts for degradation of dyes

Catalyst	Pollutants	Irradiation source	Time (min)	Degradation (%)	Ref.
$ZnCo_2O_4$–MoS_2/Ag	MB	UV light	150	95.4	40
Ag@AgCl/$ZnCo_2O_4$	Rhodamine B	Xenon 1000 W	150	99.4	41
CuO/$ZnCo_2O_4$/CNTs	Crystal violet	Tungsten 200 W	120	87.7	5
$ZnCo_2O_4$/Co_3O_4	Acid violet 7	Osram 125 W	70	93.5	42
$ZnCo_2O_4$/GO	Methyl red	Osram (400 W)	120	94.3	13
ZnO/$ZnCo_2O_4$	MB	Halogen (150 W)	75	96.5	43
S,N-CQDs/$ZnCo_2O_4$	Acid blue 113	Osram lamp (400 W)	120	93	44
$ZnCo_2O_4$/g-C_3N_4/Cu	Metronidazole	Sun light	30	98	45
$(BiO)_2CO_3$@$ZnCo_2O_4$	Indigo carmine	Halogen (150 W)	100	98.6	This work

decomposition rates are 12BiC@ZC > 18BiC@ZC > 6BiC@ZC > ZC > BiC.

3.2.1 Catalyst dosage. Fig. 5F illustrates the effect of the 12BiC@ZC catalyst dose on IC degradation. Increasing the 12BiC@ZC catalyst dose from 0.75 to 1.5 g L^{-1} enhanced the IC degradation efficiency from 85.57% (k_1 = 0.0201 min^{-1}) to 98.6% (k_1 = 0.038 min^{-1}). The concentration of IC and the visible light-simulating light source remained constant; when the catalyst dosage increased, the number of active sites also increased, enhancing the interaction rate between the catalyst and the dye molecules, elevating the photocatalytic efficiency.[19,36] However, the breakdown process of IC was impeded when the BiC@ZC catalyst dosage increased to 1.5 g L^{-1}, perhaps due to photon scattering or reflection resulting from the excess catalyst dosage.[19] A further cause may be that the turbidity of the solution escalates with the catalyst dose, restricting light exposure to the catalyst, leading to a decrease in photoactive particles and diminishing photocatalytic efficacy.[13] The 12BiC@ZC dose of 1.25 g L^{-1} has been chosen as a stable condition for assessing additional variables.

3.2.2 Initial concentration of IC. Using 12BiC@ZC loading at 1.25 g L^{-1}, pH 6.5, an adsorption time of 60 minutes, and a light irradiation time of 100 minutes, Fig. 5G shows the change in the initial IC concentration from 30 to 70 ppm. The findings indicate that an increase in the IC concentration reduces the IC decomposition efficiency of 12BiC@ZC; at an initial concentration of 30–40 ppm, 12BiC@ZC fully degrades IC within 80 minutes of light exposure. As the IC concentration increases from 40 to 70 ppm, the efficiency of IC breakdown decreases in the following order: 98.6% (k = 0.03805 min^{-1}); 89.5% (k = 0.0207 min^{-1}); and 81.4% (k = 0.0157 min^{-1}). The data demonstrate that the Langmuir–Hinshelwood first-order kinetic model accurately describes the IC breakdown process of 12BiC@ZC. As the initial concentration of IC increases, the decomposition rate constant diminishes, with the IC decomposition mostly occurring at the surface of 12BiC@ZC. A certain quantity of adsorbent can only accommodate a limited number of adsorbed molecules; hence, as the IC concentration increases, the photocatalytic efficiency of IC breakdown by 12BiC@ZC diminishes.[19,40]

3.2.3 Effect of pH. The pH of the solution has a significant impact on photocatalytic efficiency. This research examines the pH of the IC dye solution, which ranges from 4 to 10. Fig. 5H demonstrates that the pH of the IC solution at a concentration of 50 ppm was 6.5, which corresponds to the optimal IC degradation efficiency of 12BiC@ZC. The findings established the isoelectric point (pH_{PZC}) of 12BiC@ZC as 7.3. At pH 4 and 6.5, which are below the pH_{PZC}, the surface of 12BiC@ZC is positively charged, facilitating electrostatic attraction with IC^- and thereby enhancing adsorption and photocatalytic degradation efficiency. Fig. 5H indicates that the IC decomposition efficiency at pH 4 (95%; k_1 = 0.028 min^{-1}) is inferior to that at pH 6.5 (98.5%; k_1 = 0.038 min^{-1}). This is attributed to the elevated H^+ concentration at pH 4, which engenders competitive attraction interactions between the 12BiC@ZC material's surface and H^+, thereby obstructing the attraction interaction between IC^- and the surface of 12BiC@ZC.[43,46] At pH 8 and 10, which exceed the pH_{PZC}, the surface of 12BiC@ZC has a negative charge identical to that of IC^-. This leads to a repulsive interaction among the similarly charged ions, diminishing both IC adsorption capacity and the IC breakdown efficiency of 12BiC@ZC.[36]

Table 2 The correlation coefficient and rate constant values of the kinetic models for the degradation of IC over ZC and BiC@ZC

	Zero order		First order		Second order	
Sample	r^2	k_0	r^2	k_1	r^2	k_2
ZC	0.97977	−0.26012	0.99201	0.00829	0.9951	2.7567×10^{-4}
BiC	0.97514	−1.0039	0.97838	0.00245	0.98108	0.6013×10^{-4}
6BiC@ZC	0.96238	−0.42992	0.99944	0.02265	0.90684	12.7×10^{-4}
12BiC@ZC	0.93697	−0.47700	0.99901	0.03805	0.70692	88.4×10^{-4}
18BiC@ZC	0.94467	−0.44402	0.99897	0.02592	0.88427	24×10^{-4}
TiO_2	0.98986	−0.36479	0.96937	0.01909	0.80273	14.3×10^{-4}

3.2.4 Stability and reusability. Stability and reusability are crucial considerations for the practical application of photocatalytic materials. This work examined the IC degradation efficiency of 12BiC@ZC after four reuses under the previously established optimal conditions. Following the first photocatalytic reaction, the 12BiC@ZC sample was filtered, cleaned, dried at 100 °C, and then reused for the second photocatalytic reaction. The findings indicated that the IC degradation efficiency of 12BiC@ZC after four reuses was 98.6%, 94.9%, 89.9%, and 80.7%, respectively. This suggests that the nanocomposite has significant reusability. In addition, the findings demonstrated that the fundamental characteristic peaks of the 12BiC@ZC sample remained unchanged after four reuses, proving that the heteroatoms in 12BiC@ZC are very stable photocatalysts for wastewater treatment under visible light (Fig. 6A and B).

3.3 Mechanism for photocatalytic reactions

Reactive species, including $O_2^{\bullet-}$, h^+, and $^{\bullet}OH$, are essential in photocatalytic reactions. Radical quenching experiments using 1,4-benzoquinone (BQ), $Na_2C_2O_4$, and *tert*-butanol (TBA) were carried out to capture $O_2^{\bullet-}$, h^+, and $^{\bullet}OH$ species in the solution, thereby influencing the photodegradation efficiency. Fig. 7A and B illustrates that adding TBA and BQ substantially reduced the photocatalytic efficiency of IC degradation, yielding values of 54.6% ($k_1 = 0.0064\ min^{-1}$) and 52.7% ($k_1 = 0.0059\ min^{-1}$), respectively. Conversely, the addition of $Na_2C_2O_4$ resulted in a degradation efficiency of 84.5% ($k_1 = 0.0172\ min^{-1}$), representing a slight reduction relative to the conditions with no quencher. This suggests that $O_2^{\bullet-}$ and $^{\bullet}OH$ are the primary contributors to the photodegradation of IC by 12BiC@ZC.

Fig. 2C illustrates that the Tauc function estimated E_g of ZC and BiC to be 1.67 eV and 3.0 eV, respectively. The reduction potentials of the CB (E_{CB}) and VB (E_{VB}) of ZC were found to be −0.395 and 1.275 eV, respectively, and of BiC were found to be 3.375 and 0345 eV, using the formulae $E_{VB} = \chi - E_e + 0.5E_g$ and $E_{CB} = E_{VB} - E_g$.[5,47] Photogenerated electron–hole pairs are created in photocatalysis when semiconductors absorb light. These pairs subsequently react with water and O_2 is absorbed on the material surface to produce ROS, such as $O_2^{\bullet-}$ and $^{\bullet}OH$, which break down contaminants. Type-II and direct Z-schemes can describe the photocatalytic mechanism of BiC@ZC in degrading the IC dye.

(i) Type-II (Fig. 8A). In CB, ZC has an $E_{CB} = -0.395$ eV that is more negative than that of BiC ($E_{CB} = 0.345$ eV), resulting in the transfer of electrons from ZC to BiC. However, these electrons cannot reduce O_2 to $O_2^{\bullet-}$ ($E^{\circ}_{O_2/O_2^{\bullet-}} = -0.33$ eV $> E_{CB} = 0.345$ eV). At the VB, the holes of BiC migrate to ZC due to the greater positive reduction potential of BiC ($E_{CB} = 3.375$ eV) compared to that of ZC ($E_{CB} = 1.275$ eV), resulting in a combination with the holes of ZC; nonetheless, these holes lack sufficient strength to oxidize H_2O to generate $^{\bullet}OH$.

(ii) Z-scheme (Fig. 8B). Interactions occur at the heterojunction between the BiC and ZC phases, with direct recombination taking place between electrons in the CB of BiC and holes in the VB of ZC. This selective recombination results in the retention of the two most energetic particles; the remaining electrons in the CB of ZC possess a reduction potential more negative than that of $O_2/O_2^{\bullet-}$, so they can transfer electrons to O_2 to generate $O_2^{\bullet-}$. The holes in the VB of BiC have a reduction potential more positive than that of $OH^{\bullet}/H_2O$, hence facilitating the oxidation of H_2O to generate $^{\bullet}OH$.

The ROS immediately interacts with IC, resulting in chain breakdown, oxidation, and finally mineralization. As can be observed, this type-II mechanism is anticipated to fail; the potential at the VB of BiC is insufficiently negative to produce $O_2^{\bullet-}$, while the potential at the CB of ZC is inadequately positive to create $^{\bullet}OH$, resulting in diminished oxidation/reduction potential and decreased photocatalytic efficiency. Consequently, type-II will lessen the capacity to produce ROS, which contradicts the observed high photocatalytic effectiveness in experiments.

3.4 DFT calculations of the frontier HOMO–LUMO and Fukui functions of IC

3.4.1 Fukui function of IC. As demonstrated in Table 3, the coefficients include f^- for electrophilic attack, f^+ for nucleophilic attack, and f^0 for radical attack. The symbol W^- denotes the nucleophilic work function, the minimal energy necessary for a nucleophilic attack. The symbol W^+ denotes the electrophilic work function, the lowest energy necessary for

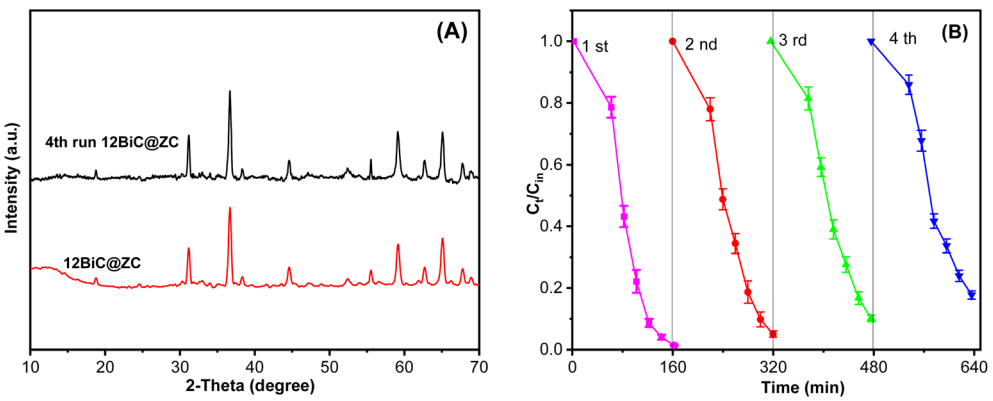

Fig. 6 (A) XRD and (B) reusability of 12BiC@ZC for 4 successive cycles.

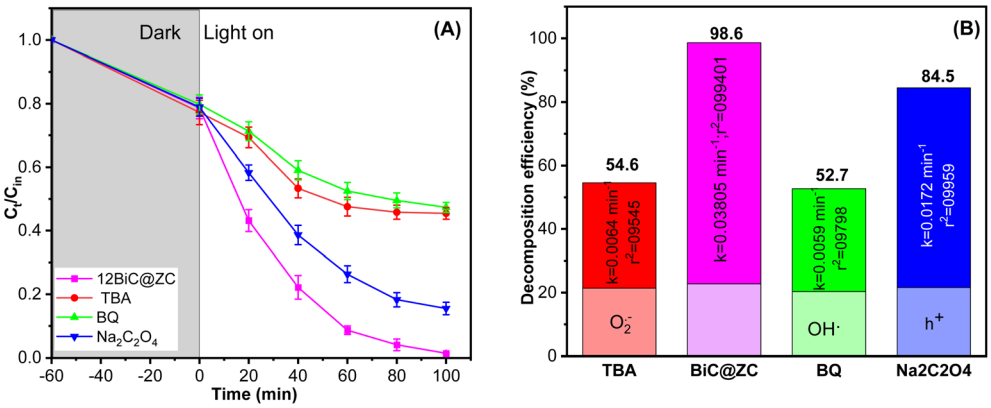

Fig. 7 (A and B) Effects of different scavengers on the IC degradation over 12BiC@ZC.

electrophilic attack. The dual-descriptor indicates susceptibility to electrophilic or nucleophilic assault, while hardness serves as a global reactivity descriptor that quantifies a chemical entity's resistance to changes in its electron distribution. Table 3 illustrates that for the carbon atom, the number 25 (line 1) exhibits a coefficient f^- with a markedly high positive value of 0.9322 (93.22%). Consequently, C-13 demonstrates superior electrophilic attack capabilities against $O_2^{\bullet-}$, as depicted in Fig. 9A. Additionally, the value of f^0 has been calculated as 0.4679 (46%), corroborating the radical attack, ˙OH, for C-13. The dual descriptor ($\Delta f = 0.0036 - 0.9332 = -0.9287$) is negative, indicating that the C-13 position favours an nucleophilic character, namely the donation of electrons to the $O_2^{\bullet-}$ molecular ion. For the local index C-13, the hardness is a low positive value of 0.0911, indicating that C-13 readily accepts electrons from $O_2^{\bullet-}$. The W^- value is 0.267, signifying the minimal energy necessary for a nucleophilic attack by $O_2^{\bullet-}$. As indicated in Table 3, line 2, the f^+ value for the nitrogen atom is 0.3743, indicating that nitrogen readily accommodates a nucleophile. Conversely, the C-26 aromatic ring has a higher f^+ value of 0.59, suggesting that it is also conducive to nucleophilic attachment. According to the analysis above, the positions in IC for nucleophile attachment are straightforward for $O_2^{\bullet-}$ and the free radical ˙OH, and the electrophile h^+ reacts at C-13, C-25, and C-26, while other positions in IC exhibit low reactivity and have been excluded.[24,48] The process of photocatalytic degradation can be explained by incorporating the heterojunction charge-transfer pathway with a DFT-based reactivity investigation of the IC molecule. Fig. 8B illustrates that the BiC@ZC heterojunction improves the efficient separation of photogenerated electron–hole pairs upon light irradiation. ˙OH and $O_2^{\bullet-}$ are the principal oxidising agents responsible for dye degradation. To clarify the molecular-level degradation pathway, a Fukui function analysis has been performed on the IC molecule. The Fukui indices of radical species were estimated. Consequently, the heterojunction architecture dictates the production and movement of reactive species. The Fukui analysis delineates the reaction sites on the dye molecule, providing a deeper understanding of the overall photocatalytic degradation mechanism.

3.4.2 Frontier HOMO–LUMO of the IC molecule. The energy parameters and electronic properties of the IC molecule, computed *via* the DFT method with the B3LYP/6-311G(d,p) basis set in a water solvent, are shown in Table 4. As

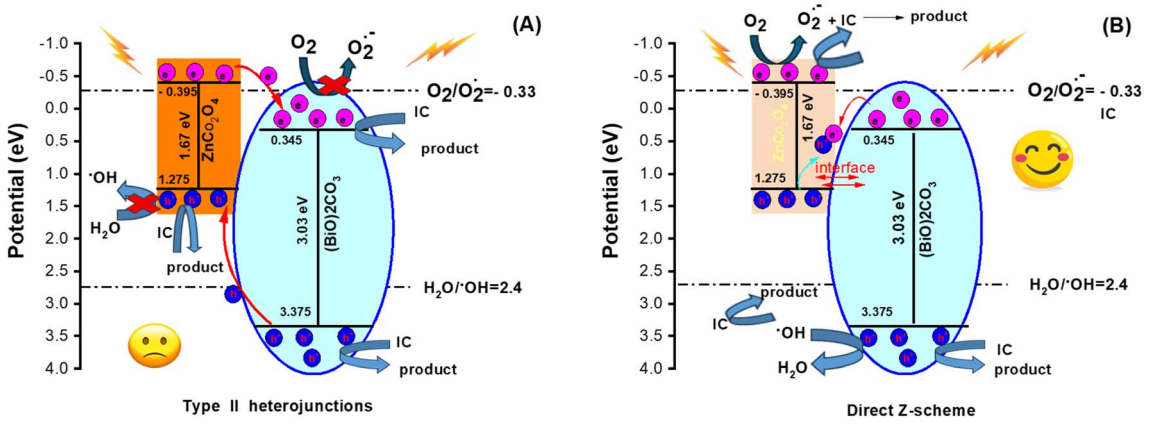

Fig. 8 Schematic diagram of the organic dye removal mechanism. (A) Traditional type-II heterojunction and (B) Z-scheme heterojunction charge transfer pathway.

Table 3 The local parameters of atoms on IC based on DFT

N	Z	f^-	f^+	f^0	Dual-descriptor	Hardness (a.u.)	W^- (eV)	W^+ (eV)
13	C	0.9322	0.0036	0.4679	−0.9287	0.0911	0.2671	0.0001
25	N	0.0011	0.3743	0.1877	0.3733	0.0019	0.0003	0.1073
26	C	0.0026	0.5609	0.2818	0.5583	0.0029	0.0007	0.1607

indicated in Table 5, the significant parameters from DFT calculations show that the total energy after SCF convergence is −2447.1968 a.u., demonstrating significant stability of the optimal state. The molecule exhibits a dipole moment of 3.07 debye, indicating considerable polarization due to the electronegative sulfonate group ($-SO_3^-$) attached to the conjugated system in IC. The energy levels of the frontier orbitals were established as $E_{HOMO} = -5.667$ eV and $E_{LUMO} = -3.233$ eV, resulting in an energy gap of $\Delta E_g = 2.434$ eV. The minimal energy gap signifies that indigo carmine is a soft molecule, excited by electrons, and exhibits an excellent ability to interact with visual radiation. According to the Koopmans theory, the ionisation energy, IE = 5.667 eV and electron affinity, EA = 3.233 eV have been used to calculate the global hardness, $\eta = 2.434$ eV, chemical potential, $\mu = -4.672$ eV, electronegativity, $\chi = 4.672$ eV, global softness, $S = 0.4108$ eV^{-1}, and electrophilicity index, $\omega = 4.484$ eV.[24,49,50] The negative μ and relatively high χ values suggest that the molecule exhibits an average tendency to attract electrons, indicating that it has a high electronegativity index. $\eta = 2.434$ eV (which suggests moderate hardness) and $S = 0.4108$ eV^{-1} (indicating moderate softness) demonstrate that the molecule shows neither extreme hardness nor extreme softness. IC is susceptible to the simple transfer of charged particles but is not highly inert. The ω value of 4.484 eV indicates a moderately high electrophilicity, suggesting that the molecule may function as an electrophile in specific contexts. The evaluation of the work functions, with $W^- = 3.455$ eV, is significantly lower than that of $W^+ = 5.889$ eV. A lower W^- indicates that the molecule can more readily donate electrons, functioning as a nucleophile, compared to its ability to accept electrons, as electrophilic attack necessitates greater energy input. Despite a moderate ω, the relative ratio of W^+/W^- suggests that the molecule is more likely to function as an electron donor, exhibiting nucleophilic behaviour under various conditions.

As seen in Table 4, line 1 and Fig. 9B, the HOMO and LUMO indicate a primary concentration of electrons in the HOMO on the π-conjugated system of the aromatic rings in IC, whereas the LUMO reaches towards the sulfonate groups $-SO_3^-$. The transfer of electron density from the chromophore (donor) to the electronegative substituent (acceptor) region indicates the existence of intramolecular charge transfer (ICT) upon electronic excitation. As calculations presented in Table 4, some major transitions from HOMO to LUMO, such as 118 to 119, 117 to 119, 116 to 119, 115 to 119, 118 to 120 and 117 to 120 (among energy transitions, the HOMO−118 to LUMO−119 level has the lowest excitation energy of 2.436 eV ($\lambda \approx 509$ nm)), are positioned within the visible spectrum and correspond to the characteristic blue color of indigo carmine, as observed in the experimental absorption spectrum ($\lambda_{max} = 610$ nm). The frontier molecular orbitals (HOMO–LUMO) method applied to the IC molecule has a similar conformation to that of IC in the previous article.[51] A larger basis set (6-311G(d,p)), compared to many older studies, along with the inclusion of a solvent, provides a more accurate representation of IC in an aqueous environment. Time-dependent density functional theory (TD-DFT) has been employed to enhance the accuracy of excited-state calculations. $\Delta E = 2.436$ eV is more accurate and

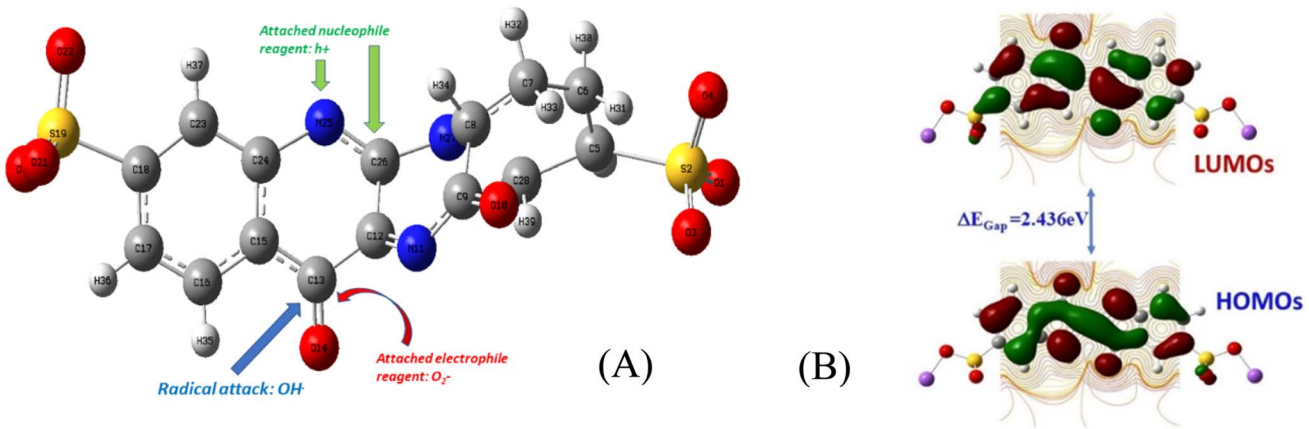

Fig. 9 (A) The structure of IC is presented using Gaussian View 9.0. (B) HOMO−118–LUMO−119 MO of IC (DFT method level: B3LYP/6-311G(d,p); SMD-water).

Table 4 Characteristic electron transitions of HOMO–LUMO computed using DFT/TD-DFT at the B3LYP/6-311G(d,p) level in an aqueous solvent (SMD model) for the IC molecule

MOs	Electron transition MO	E_{HOMO}, eV	E_{LUMO}, eV	ΔE_{Gap}, eV	Wavelength, λ (nm)
118 → 119	**HOMO → LUMO**	**−5.666**	**−3.230**	**2.436**	**509.039**
117 → 119	HOMO−1 → LUMO	−6.671	−3.230	3.441	360.373
116 → 119	HOMO−2 → LUMO	−6.913	−3.230	3.683	336.676
115 → 119	HOMO−3 → LUMO	−6.973	−3.230	3.743	331.316
118 → 120	HOMO → LUMO+1	−5.666	−1.757	3.909	317.201
117 → 120	HOMO−1 →LUMO+1	−6.671	−1.757	4.914	252.335

Table 5 Parameters and results from DFT calculations for IC (job: SP, level: B3LYP/6-311G(d,p), and SMD-water)

Parameter	Value	Note
E(SCF)	−2447.1968 a.u.	
Basic set	6-311G(d,p)	
Solvent	Water	SCRF=(SMD, solvent=water)
Dipole moment	3.0707 D	
E_{HOMO}	−0.20823 a.u. = −5.667 eV	Eigenvalue HOMO
E_{LUMO}	−0.1187 a.u. = −3.233 eV	Eigenvalue LUMO
$\Delta E = E_{LUMO} - E_{HOMO}$	2.436 eV	
Ionization energy, IE	5.667 eV	IE = $-E_{HOMO}$
Electron affinity, EA	3.233 eV	EA = E_{LUMO}
Hardness, η	2.434 eV	$\eta = E_{LUMO} - E_{HOMO}$
Chemical potential, μ	−4.672 eV	$\mu = (E_{HOMO} + E_{LUMO})/2$
Electronegativity, χ	4.672 eV	$\chi = -\mu$
Global softness, S	0.4108 eV^{-1}	$S = 1/\eta$
Electrophilicity index, ω	4.484	$\omega = \mu^2/(2\eta)$
Electrophilic work function, W^+	5.889 eV	$W^+ = -\mu + \eta/2$
Nucleophilic work function, W^-	3.455 eV	$W^+ = -\mu - \eta/2$

correlates more closely with experimental data compared to the gas-phase published data. Our DFT/TD-DFT calculations, employing the B3LYP/6-311G(d,p) method in an aqueous solvent, yield a more accurate and experimentally consistent HOMO–LUMO gap for IC compared to previous studies. However, additional refinements, including the use of diffuse basis sets, long-range corrected functionals, and explicit solvation, could increase accuracy more significantly.[52–54]

4. Conclusions

This study synthesized a novel BiC@ZC heterojunction to enhance the photocatalytic activity under visible light. BiC was uniformly distributed across the ZC surface at mass ratios of 6%, 12%, and 18%, respectively. The experimental findings indicated that BiC@ZC effectively treats IC solution under visible light, with 12BiC@ZC identified as the most effective in dye treatment. The IC degradation efficiency of 12BiC@ZC attained 98.6% with a catalyst loading of 1.25 g L^{-1}, an initial IC concentration of 50 ppm, an adsorption duration of 60 minutes, and a light irradiation period of 100 minutes. Zero-order, first-order, and second-order kinetic equations were formulated exhibiting high coefficients of determination for the IC breakdown process of BiC@ZC. The first-order kinetic equation is most appropriate when r_1^2 = 0.97838–0.99901. The catalytic mechanism of the IC breakdown process of BiC@ZC was ascertained, whereby the free radicals $O_2^{\bullet-}$ and $^{\bullet}OH$ serve as the principal agents. The BiC@ZC heterojunction exhibits significant durability and stability after four cycles of reuse. These are catalysts with the potential for practical use in treating hazardous organic pollutants under sunlight. DFT–Fukui analysis indicates that the IC molecule donates electrons and therefore acts as a nucleophilic reagent. In addition, work-function calculations (W^+, global index) together with DFT/TD-DFT simulations using the B3LYP/6-311G(d,p) level of theory in aqueous solution yield a more accurate and experimentally consistent HOMO–LUMO gap for IC compared with previous reports.

Conflicts of interest

The authors claim that they have no known competing interests that could impact the research described in this publication.

Data availability

Data for this article, including supporting data related to the photocatalytic degradation of indigo carmine over the $(BiO)_2CO_3$@$ZnCo_2O_4$ heterojunction, are available at Figshare at https://doi.org/10.6084/m9.figshare.31082098.

Acknowledgements

This research was supported by the Industrial University of Ho Chi Minh City (IUH) under grant number 85/HD-DHCN (25BCNHH05) dated 22/12/2025.

References

1 N. T. Mai Tho, N. Van Cuong, V. H. Luu Thi, N. Q. Thang and P. H. Dang, *RSC Adv.*, 2023, **13**, 16248–16259.
2 L. S. Alqarni, M. N. Goda, A. Albadri, K. K. Taha, A. A. Alharbi, M. Ismail and A. Modwi, *Diamond Relat. Mater.*, 2025, **160**, 113055.
3 G. K. Sukhadeve, S. Y. Janbandhu, R. Kumar, D. H. Lataye, D. D. Ramteke and R. S. Gedam, *Ceram. Int.*, 2022, **48**, 29121–29135.
4 F. T. Geldasa, M. A. Kebede, M. W. Shura and F. G. Hone, *RSC Adv.*, 2023, **13**, 18404–18442.
5 N. Alomayrah, M. Ikram, S. Zulfiqar, S. Alomairy, M. S. Al-Buriahi, I. Shakir, M. F. Warsi and E. W. Cochran, *RSC Adv.*, 2024, **14**, 24874–24897.
6 H. Wang, L. Zhang, Z. Chen, J. Hu, S. Li, Z. Wang, J. Liu and X. Wang, *Chem. Soc. Rev.*, 2014, **43**, 5234–5244, DOI: 10.1039/c4cs00126e.
7 D. Renuka Devee, T. Sivanesan, R. M. Muthukrishnan, D. Pourkodee, P. Mohammed Yusuf Ansari, S. M. Abdul Kader and R. Ranjani, *Chem. Phys. Impact*, 2024, **8**, 100605, DOI: 10.1016/j.chphi.2024.100605.
8 N. D. Dien, T. T. H. Pham, X. H. Vu, V. T. Xuan, T. T. T. Nguyen, T. T. Trang, N. Van Hao, P. T. Nga, T. T. Kim Chi, T. T. H. Giang and N. D. Toan, *RSC Adv.*, 2024, **14**, 28244–28259.
9 M. Cheng, G. Zeng, D. Huang, C. Lai, P. Xu, C. Zhang and Y. Liu, *Chem. Eng. J.*, 2016, **284**, 582–598.
10 L. Schumacher and R. Marschall, *Top. Curr. Chem.*, 2022, **380**, 53, DOI: 10.1007/s41061-022-00406-5.
11 D. Tian, H. Zhou, H. Zhang, P. Zhou, J. You, G. Yao, Z. Pan, Y. Liu and B. Lai, *Chem. Eng. J.*, 2022, **428**, 131166, DOI: 10.1016/j.cej.2021.131166.
12 M. I. A. Abdel Maksoud, G. S. El-Sayyad, N. Mamdouh and W. M. A. El Rouby, *J. Inorg. Organomet. Polym. Mater.*, 2022, **32**, 3621–3639.
13 S. A. Ehsanizadeh, M. Ahmadi-Kashani, Z. H. Abdulhusain, M. J. Abed and M. Salavati-Niasari, *Appl. Water Sci.*, 2025, **15**, 128.
14 R. Jahanshahi, H. H. Moghadam, S. Sobhani and J. M. Sansano, *RSC Adv.*, 2024, **14**, 26424–26436.
15 J. Chen, J. Zhan, Y. Zhang and Y. Tang, *Chin. Chem. Lett.*, 2019, **30**, 735–738.
16 B. Tan, Y. Fang, Q. Chen, X. Ao and Y. Cao, *Opt. Mater.*, 2020, **109**, 110470.
17 M. Amiri and H. Mahmoudi-Moghaddam, *Microchem. J.*, 2021, **160**, 105663.
18 H. Benhebal, C. Wolfs, S. Kadi, R. G. Tilkin, B. Allouche, R. Belabid, V. Collard, A. Felten, P. Louette, S. D. Lambert and J. G. Mahy, *Inorganics*, 2019, **7**, 77.
19 S. Huang, Y. Wu, Q. Zhang, X. Jin, D. Li, H. Liu, P. Chen, W. Lv and G. Liu, *Environ. Sci.: Nano*, 2022, **9**, 2104–2120.
20 Y. L. Qin, Y. Q. Wang, P. Y. Zhao, X. Y. Liu, Z. Y. Liu, D. R. Ni, B. L. Xiao and Z. Y. Ma, *Appl. Phys. A: Mater. Sci. Process.*, 2022, **126**, 851.
21 C. Zhou, X. li Wang, H. Yu, M. Yang, X. ting Dong and Y. Yang, *Appl. Organomet. Chem.*, 2024, **38**, e7728.
22 J. Li, Q. Shi, L. Ha, Y. Sun and H. Shi, *J. Mater. Sci.*, 2025, **60**, 7247–7258.
23 R. Pucci and G. G. N. Angilella, *Found. Chem.*, 2022, **24**, 59–71.
24 P. Geerlings, F. De Proft and W. Langenaeker, *Chem. Rev.*, 2003, **103**, 1793–1874.
25 R. Pucci and G. G. N. Angilella, *Found. Chem.*, 2022, **24**, 59–71.
26 K. Michalec, B. Mozgawa, A. Kusior, P. Pietrzyk, Z. Sojka and M. Radecka, *J. Phys. Chem. C*, 2024, **128**, 5011–5029.
27 X. Wang, P. Wu, Z. Zhao, L. Sun, Q. Deng, Z. Yin and X. Chen, *J. Mater. Sci.: Mater. Electron.*, 2020, **31**, 4895–4904.
28 Q. Zhang, F. Xie, J. Wang, T. Wang, J. Lei, W. Li, J. Cheng and Y. Zhang, *Appl. Organomet. Chem.*, 2024, **38**, e7614.
29 G. Guo and H. Yan, *Chem. Phys.*, 2020, **538**, 110920.
30 W. Zhang, C. Xu, E. Liu, J. Fan and X. Hu, *Appl. Surf. Sci.*, 2020, **515**, 146039.
31 F. Wang, S. Zhan, F. Zhou, Q. He, C. Zhang, J. Lai and Y. Song, *J. Environ. Chem. Eng.*, 2022, **10**, 107576.
32 M. I. Abd-Elrahman, L. Rashad, H. A. Mohamed, Y. A. Taya and A. A. El-Fadl, *J. Inorg. Organomet. Polym. Mater.*, 2025, **35**, 3857–3864.
33 K. Yang, Y. Zhang, C. Meng, F. F. Cao, X. Chen, X. Fu, W. Dai and C. Yu, *Appl. Surf. Sci.*, 2017, **391**, 635–644.
34 H. Guo, J. Chen, W. Weng, Q. Wang and S. Li, *Chem. Eng. J.*, 2014, **239**, 192–199.
35 Y. Gao, T. Cao, J. Du, X. Qi, H. Yan and X. Xu, *Catalysts*, 2025, **15**, 56.
36 N. H. Nam, N. Q. Hung, N. T. H. Anh, N. Q. Thang and N. T. M. Tho, *RSC Adv.*, 2024, **14**, 32436–32450.
37 J. Li, Q. Shi, L. Ha, Y. Sun and H. Shi, *J. Mater. Sci.*, 2025, **60**, 7247–7258.
38 G. Zhou, Z. Lu, X. Liu, M. Song, G. Xing, X. Zhu, Z. Yu, L. Xu, P. Huo and Y. Yan, *Inorg. Chem. Commun.*, 2020, **111**, 107630.
39 N. T. M. Tho and M. A. Tran Nguyen, *RSC Adv.*, 2025, **15**, 25839–25853.
40 M. I. A. Abdel Maksoud, G. S. El-Sayyad, N. Mamdouh and W. M. A. El Rouby, *J. Inorg. Organomet. Polym. Mater.*, 2022, **32**, 3621–3639.
41 W. Liu, S. Hu, Y. Wang, B. Zhang, R. Jin and L. Hu, *Nanoscale Res. Lett.*, 2019, **14**, 108.
42 S. A. Heidari-Asil, S. Zinatloo-Ajabshir, H. A. Alshamsi, A. Al-Nayili, Q. A. Yousif and M. Salavati-Niasari, *Int. J. Hydrogen Energy*, 2022, **47**, 16852–16861.
43 N. T. M. Tho, T. T. Ha, N. Van Cuong, T. V. M. Sreekanth and P. H. Dang, *Arabian J. Sci. Eng.*, 2024, **49**, 7961–7977.
44 R. Behnood and G. Sodeifian, *J. Photochem. Photobiol., A*, 2021, **405**, 112971.

45 R. Jahanshahi, A. Mohammadi, M. Doosti, S. Sobhani and J. M. Sansano, *Environ. Sci. Pollut. Res.*, 2022, **29**, 65043–65060.
46 R. Abdel-Aziz, M. A. Ahmed and M. F. Abdel-Messih, *J. Photochem. Photobiol., A*, 2020, **389**, 112245.
47 B. Zhu, Q. Dong, J. Huang, D. Song, L. Chen, Q. Chen, C. Zhai, B. Wang, J. J. Klemeš and H. Tao, *RSC Adv.*, 2023, **13**, 1594–1605.
48 J. C. Hackett, *J. Am. Chem. Soc.*, 2010, **132**(21), 7558.
49 D. Chakraborty and P. K. Chattaraj, *Chem. Sci.*, 2021, **12**, 6264–6279, DOI: 10.1039/d0sc07017c.
50 P. K. Chattaraj, U. Sarkar and D. R. Roy, *Chem. Rev.*, 2006, **106**, 2065–2091.
51 M. A. M. El-Mansy, *Spectrochim. Acta, Part A*, 2017, **183**, 284–290.
52 D. Jacquemin, I. Duchemin and X. Blase, *J. Chem. Theory Comput.*, 2015, **11**, 5340–5359.
53 S. J. Pitman, A. K. Evans, R. T. Ireland, F. Lempriere and L. K. McKemmish, *J. Phys. Chem. A*, 2023, **127**, 10295–10306.
54 V. V. Volkov, R. Chelli, R. Righini and C. C. Perry, *Dyes Pigm.*, 2020, **172**, 107761.